Magnetic Resonance Materials in Physics, Biology and Medicine
https://doi.org/10.1007/s10334-024-01159-6

RESEARCH ARTICLE

Spatial profiling of in vivo diffusion-weighted MRI parameters in the healthy human kidney

Nima Gilani[1] · Artem Mikheev[1] · Inge M. Brinkmann[2] · Malika Kumbella[1] · James S. Babb[1] · Dibash Basukala[1] · Andreas Wetscherek[3] · Thomas Benkert[4] · Hersh Chandarana[1] · Eric E. Sigmund[1]

Received: 20 October 2023 / Revised: 17 January 2024 / Accepted: 26 March 2024

Abstract

Objective Diffusion-weighted MRI is a technique that can infer microstructural and microcirculatory features from biological tissue, with particular application to renal tissue. There is extensive literature on diffusion tensor imaging (DTI) of anisotropy in the renal medulla, intravoxel incoherent motion (IVIM) measurements separating microstructural from microcirculation effects, and combinations of the two. However, interpretation of these features and adaptation of more specific models remains an ongoing challenge. One input to this process is a whole organ distillation of corticomedullary contrast of diffusion metrics, as has been explored for other renal biomarkers.

Materials and methods In this work, we probe the spatial dependence of diffusion MRI metrics with concentrically layered segmentation in 11 healthy kidneys at 3 T. The metrics include those from DTI, IVIM, a combined approach titled "REnal Flow and Microstructure AnisotroPy (REFMAP)", and a multiply encoded model titled "FC-IVIM" providing estimates of fluid velocity and branching length.

Results Fractional anisotropy decreased from the inner kidney to the outer kidney with the strongest layer correlation in both parenchyma (including cortex and medulla) and medulla with Spearman correlation coefficients and p-values (r, p) of (0.42, <0.001) and (0.37, <0.001), respectively. Also, dynamic parameters derived from the three models significantly decreased with a high correlation from the inner to the outer parenchyma or medulla with (r, p) ranges of (0.46–0.55, <0.001).

Conclusions These spatial trends might find implications for indirect assessments of kidney physiology and microstructure using diffusion MRI.

Keywords MRI · IVIM · Renal imaging · Microstructure · Microvasculature · DTI

Introduction

Quantitative MRI techniques such as diffusion-weighted imaging (DWI) have diagnostic and prognostic potential in a variety of renal diseases such as chronic kidney disease, polycystic kidney disease, and transplant malfunction [1]. The diffusion-weighted signal is sensitive to multiple aspects of renal function and microstructure, including tubular and vascular flow/volume, and renal interstitium [2, 3].

Within the DWI literature, the kidney microstructure is less explored compared to other organs such as the brain or prostate [4]. This is in part due to image quality challenges from echo-planar imaging artifacts [5] in the presence of respiratory and cardiac motion [6], in addition to the effect of cardiac cycle pulsatility on the diffusion

✉ Nima Gilani
nima.gilani@nyulangone.org

Eric E. Sigmund
eric.sigmund@nyulangone.org

1 Department of Radiology, Center for Advanced Imaging Innovation and Research (CAI2R), Center for Biomedical Imaging, NYU Langone Health, New York, USA

2 Siemens Healthcare GmbH, Erlangen, Germany

3 Joint Department of Physics, The Institute of Cancer Research and The Royal Marsden NHS Foundation Trust, London, UK

4 MR Application Predevelopment, Siemens Healthcare GmbH, Erlangen, Germany

Published online: 04 May 2024

Table 1 MR acquisition parameters of this study

Scan	TR/TE (ms)	Flip angle (°)	Matrix	Resolution (mm)	Orientation	Encodings	Notes
T2w HASTE	1000/91	120	320/320/20	1.1/1.1/5	Oblique coronal	–	–
PC-MRI	32.82/3.56	26	198/256/1	1.6/1.6/10	Oblique sagittal	24–27 phases	Venc: 80 cm/s
EPI-DWI	2800/(81 or 120)	90	192/192/1	2.2/2.2/5	Oblique coronal	*b*-values: 0, 10, 30, 50, 70, 80, 100, 120, 200, 400, 600, and 800 s/mm^2 12 directions	- At the systolic cardiac phase - Bipolar/flow compensated pulse sequences

EPI echo-planar imaging, *DWI* diffusion-weighted imaging, *PC-MRI* phase contrast MRI, *T2w* T2-weighted, *TR* repetition time, *TE*: echo time, *venc* velocity encoding

signal [3, 7–12]. By mitigating these artifacts exploration of the kidney microstructure might become progressively more feasible.

Macroscopically, the kidney anatomy is composed of the medulla and cortex, which are tissue types with distinct microstructures and microcirculation. Nephrons progressively perform blood filtration and reabsorption, beginning at vascular glomeruli, proceeding through the proximal convoluted tubules of the cortex, through aligned loops of Henle in the medulla, back through the distal convoluted tubules, and into the collecting duct [13]. Each of these aspects possesses features of flow, microstructural diffusion restricting features [14], anisotropy, and permeability [15], that impact water diffusion as measured in diffusion MRI.

Many studies employed variants of diffusion-weighted imaging (DWI) in vivo using intravoxel incoherent motion (IVIM), diffusion tensor imaging (DTI), and multi-component methods to characterize renal function [3, 6–12, 16–28]. IVIM [16] separates and approximates microcirculation (vascular and tubular flow) and microstructure. DTI [29] quantifies fractional anisotropy (FA) which is more prevalent in the oriented medullary bundles of tubules and collecting ducts than in the randomly oriented tubules and vasculature in the "cortical labyrinth" [19–21]. Several recent studies [24–26] also observed anisotropy of the flow component. Time-dependent diffusion MR methods similar to prior work in the prostate [30] allowed estimations of tubular diameters in combination with Monte Carlo diffusion simulations [3]. Finally, a multiple encoded FC-IVIM method [27] including a combination of conventional and flow-compensated diffusion gradient waveforms, multiple diffusion times, and Monte Carlo simulations model might enable a more detailed characterization of flow in the renal tissue [31].

Macroscopic segmentation strategies are evolving to better assess intra-organ functional variations. Piskunowicz et al. [32] performed semi-automated layered segmentations to measure ΔT2* values for blood oxygen level dependent (BOLD) imaging for chronic kidney disease (CKD) characterization. This was followed by a more automated 12-layer concentric object method (TLCO) [33], which enabled better differentiation of CKD kidneys from controls compared to the classical cortex and medulla segmentations [34]. Recently, the TLCO was applied to the analysis of apparent diffusion coefficient (ADC) [35] and arterial spin labeling (ASL) parameters [36].

In this work, we extended the concentrically layered segmentation to DTI and IVIM parameters of the healthy human kidney, as well as the multiple encoded FC-IVIM approach [27] to investigate their spatial dependency and hypothetically interpret tissue features at each concentric layer.

Methods

Imaging and preprocessing

In this HIPAA-compliant and IRB-approved prospective study, seven healthy volunteers (three male, age 26.8 ± 2.9 years, body mass index 24.2 ± 2.0) provided written informed consent prior to imaging. The volunteers underwent abdominal imaging in a 3 T MRI system (MAGNETOM Prisma; Siemens Healthcare, Erlangen, Germany) in supine position with posterior spine array (4–6 elements activated) and anterior 18 channel body matrix array receive RF coils, 4 ECG chest leads (Siemens Healthineers) for cardiac gating and scanner body coil RF transmission. Table 1 summarizes pulse sequence parameters employed in this study. Coronal oblique T2-weighted HASTE images were collected for anatomical reference. Sagittal phase-contrast (PC) MRI images through the left renal artery were collected at multiple cardiac phases to estimate the systolic cardiac phase for kidney tissue. A research application vendor-provided work-in-progress single shot echo-planar imaging sequence with dynamic field correction, and cardiac triggered oblique coronal was used for DWI acquisitions. Images were aligned to the prior HASTE imaging, and acquisitions were at multiple echo times for each of bipolar and flow compensated pulse sequences with TR/TE_1/TE_2 2800/81/120 ms, matrix 192/192/1, resolution

2.2/2.2/5 mm, GRAPPA acceleration factor 2, bandwidth 2170 Hz/pixel, and *b*-values of 0, 10, 30, 50, 70, 80, 100, 120, 200, 400, 600, and 800 s/mm^2 in 12 directions. The four DWI acquisitions (two echo times for each of bipolar and flow-compensated acquisitions) were each performed in 6 min totaling 24 min. Additionally, to correct for motion and field inhomogeneity, 16 right-to-left and 16 left-to-right phase-encoding $b=0$ images were acquired sampling the full range of motion for each kidney. Marchenko-Pasteur principal component analysis (MPPCA) [37] was performed for denoising. The kidneys were registered retrospectively to correct for breathing and cardiac motion. The processing for the left and right kidney was performed independently to better mitigate asynchronous left and right kidney motion and left-sided cardiac signal drop-out. In order to correct for field-inhomogeneity artifacts, the images were inputted into FSL TOPUP [38]. The processing flowchart was a replica of the one in Gilani et al. [6]. Image by image inspections were performed to exclude corrupted images for DTI and IVIM analysis. 3 left kidneys were excluded due to substantial signal loss [39] or unsuccessful FSL TOPUP correction, resulting in the inclusion of 11 out of 14 kidneys in the analysis.

Layered segmentation

The four DWI acquisitions were registered together with a rigid body mutual information-based algorithm and underwent a six-layer segmentation implemented as multiple zones concentric objects (MZCO) generation; both of these steps used the freely available software package FireVoxel (build 421, https://firevoxel.org/). The inner and outer borders of the kidney were manually prescribed and the MZCO algorithm mapped layers of equal thickness. The contours for these layers smoothly varied parallel to the prescribed inner and outer borders for segmentation of the kidney images containing both the medulla and cortex. Additionally, another layered segmentation mask was generated by the overlap of the layers derived above with a highly inclusive medulla segmentation based on hyperintense regions of the FA map.

Extraction of diffusion parameters

The bipolar diffusion-weighted images were processed in custom code written in MATLAB and Statistics Toolbox (Release 2022a, The MathWorks, Inc., Natick, Massachusetts, United States).

First, average IVIM maps were generated from biexponential fits of the directionally averaged bipolar gradient diffusion-weighted image sets at TE = 81 ms:

$$\frac{S}{S_0} = f_p \exp\left(-b \cdot D_p\right) + \left(1 - f_p\right) \exp\left(-b \cdot D_t\right) \tag{1.1}$$

where D_t is defined as diffusion coefficient of water in the tissue, f_p is the fraction of DWI signal that is affected by perfusion, and D_p is pseudo-diffusion coefficient which is sensitive to flow speed and architecture [2]. D_t and f_p values were determined in a first fit to high *b*-values ($b > 200$ s/mm^2) and provided as first estimates. A second fit on all *b*-values with constrained D_t was performed to estimate f_p and D_p. This approach is defined as segmented biexponential fit.

Secondly, the directional DWI signals from the bipolar acquisition at TE = 81 ms were processed analogously to the Renal Flow and Microstructure AnisotroPy (REFMAP) approach [3] to extract DTI, IVIM, and directional IVIM parameters: FA, mean (MD), axial ($D_\parallel$), radial ($D_\perp$) diffusivities, scalar *f with the same definition as* f_p, and mean (D^*), axial ($D^*_\parallel$), radial ($D^*_\perp$) pseudodiffusion coefficients. First, the *b*-value dependence of each voxel and direction was fit to a biexponential model in a segmented fashion as above. The structural diffusivities (D_t) were fit to a standard diffusion tensor model to derive $D_\parallel$, $D_\perp$, and MD as well as FA [40, 41]. Next, at each voxel, pseudo-diffusion coefficient (D_p) were projected along the already derived axial and radial eigenvectors for D_t to derive its axial ($D^*_\parallel$), radial ($D^*_\perp$), and mean (D^*) versions. The final parameter set included DTI metrics (MD, FA, $D_\parallel$, $D_\perp$) from the D_t, as well as the scalar *f*, in addition to D^*, $D^*_\parallel$, and $D^*_\perp$.

Finally, both bipolar and flow-compensated diffusion signals at both echo times, were averaged over all directions and used to generate signal intensity curves from each layer for input into the multiple encoded FC-IVIM method to estimate flow velocity *v*, vessel segment length *l*, and *f* [27] for each layer. In this process, high *b*-values from the bipolar TE 81 ms acquisition were again fitted to generate estimates of D_t, and f_p which initialized their values in a combined fit of the FC-IVIM expression to all *b*-values. A laminar flow description was adopted for the distribution of velocities in each segment of the circulatory network, and the bulk diffusivity value for flowing spins was set to 2.15 μm^2/ms. This higher value was chosen over that of pure blood (1.6 μm^2/ms [42]) to reflect the significant contribution from tubular fluid. This selection, while approximate, is also deemed acceptable given the typically much larger pseudodiffusion coefficients (by a factor of 10) to which this term serves as a background.

Statistical analysis

Spearman correlations were used to assess the association of the parameters with layers. All statistical tests in this study were conducted at the two-sided 5% significance level using SAS 9.4 software (SAS Institute, Cary, NC).

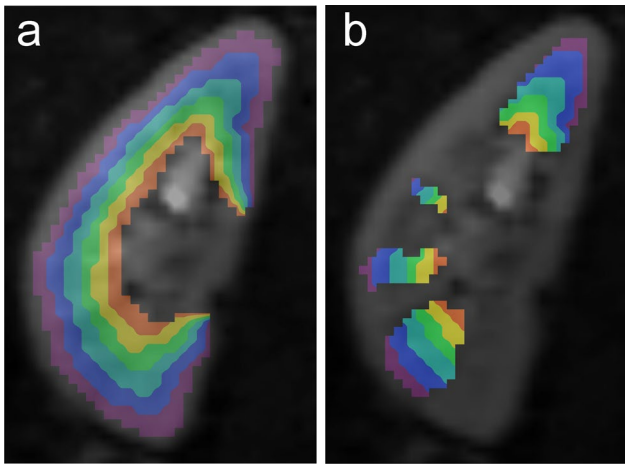

Fig. 1 **(a)** A sample kidney divided into six layers using the multiple zones concentric objects generation method of FireVoxel. **(b)** The same kidney and layers limited to a medullary region of interest highlighted based on fractional anisotropy (FA) map

Results

Figure 1 shows a sample kidney divided into six layers using the multiple zones concentric objects generation method in both full parenchymal and medullary only segmentations. Figure 2 shows a $b=0$ image, and maps of IVIM (D_t, f_p, and D_p) and DTI (MD, FA, $D_{\parallel}$, and $D_{\perp}$) parameters corresponding to the same subject. Similar maps for another kidney are shown in Supplementary Fig 1. Figure 3 shows boxplots of the group distribution of values of DTI (a), IVIM (b), and FC- IVIM (c) parameters against cortex and medulla inclusive parenchymal kidney layers (increasing layer # corresponding to outward layer progression). Figure 4 shows variation of the same parameters within medulla segmentations (derived from the FA maps) on the same kidney layers.

Table 2 summarizes Spearman correlations of the parameters separately in parenchyma (including both medulla and cortex) and pure medulla against the six layers. Most of the parameters showed significant changes from the inner to outer layers with a few exceptions. These trends can be summarized as microstructural parameters (D, MD, D_t, $D_{\parallel}$, $D_{\perp}$, FA, l) or dynamic flow parameters (f_p, f, D_p, $D^*_{\parallel}$, $D^*_{\perp}$, and v). The structurally sensitive diffusivities D, MD, D_t, and most pronouncedly perpendicular diffusivity $D_{\perp}$, all increased from the inner layers to the outer layers of the kidney, while FA decreased from the inner to outer layers. These trends were similar in the whole parenchymal and medullary segmentations, but the structural diffusivity correlations (MD, D_t, D, and especially $D_{\perp}$) were stronger, and the FA correlations weaker, in the medullary segmentation case. Conversely, in both the parenchymal and medullar layers, $D_{\parallel}$ and l were not significantly associated with layers. Dynamic IVIM parameters f_p and D_p, and FC-IVIM parameters f and flow velocity v had decreasing trends from the inner to outer layers.

Figure 5 summarizes the values of Spearman correlation coefficients (r) for each parameter for both the parenchymal) and the medullary segmentations. The figure highlights that D_p derived from IVIM, its directional variants $D^*_{\parallel}$ and $D^*_{\perp}$, and v derived from the FC-IVIM model have the highest correlations ranging from 0.46 to 0.55 in the category of dynamic parameters [2]. FA in both the parenchymal and medullary segmentations are highly layer dependent [3].

Discussion

There is a well-developed literature on preclinical murine and excised human kidney microstructure using in vivo or ex vivo modalities and their combinations such as MRI

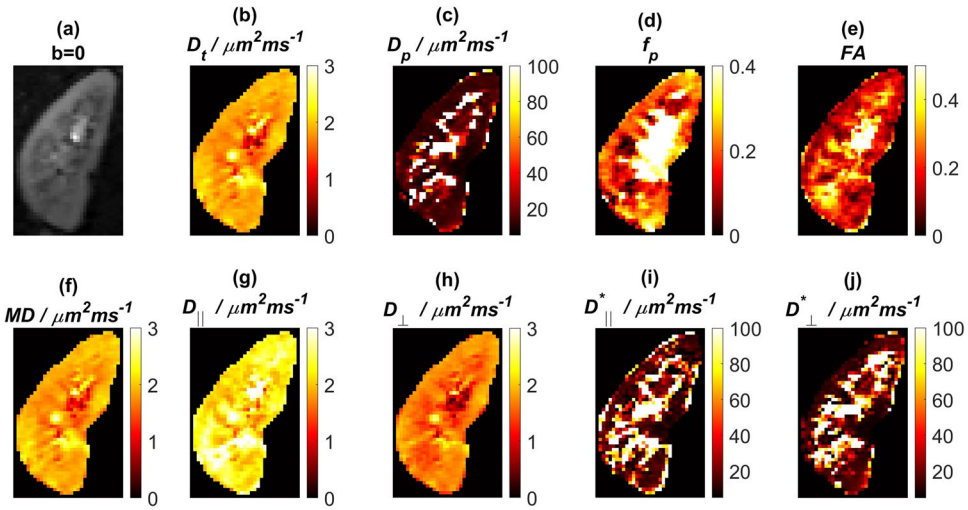

Fig. 2 A sample $b=0$ image (**a**), IVIM maps D_t (**b**), D_p (**c**), and f_p (**d**), and DTI maps *FA* (**e**), *MD* (**f**), $D_{\parallel}$ (**g**), $D_{\perp}$ (**h**), $D^*_{\parallel}$ (**i**), and $D^*_{\perp}$ (**j**), all corresponding to the same subject as in Fig. 1

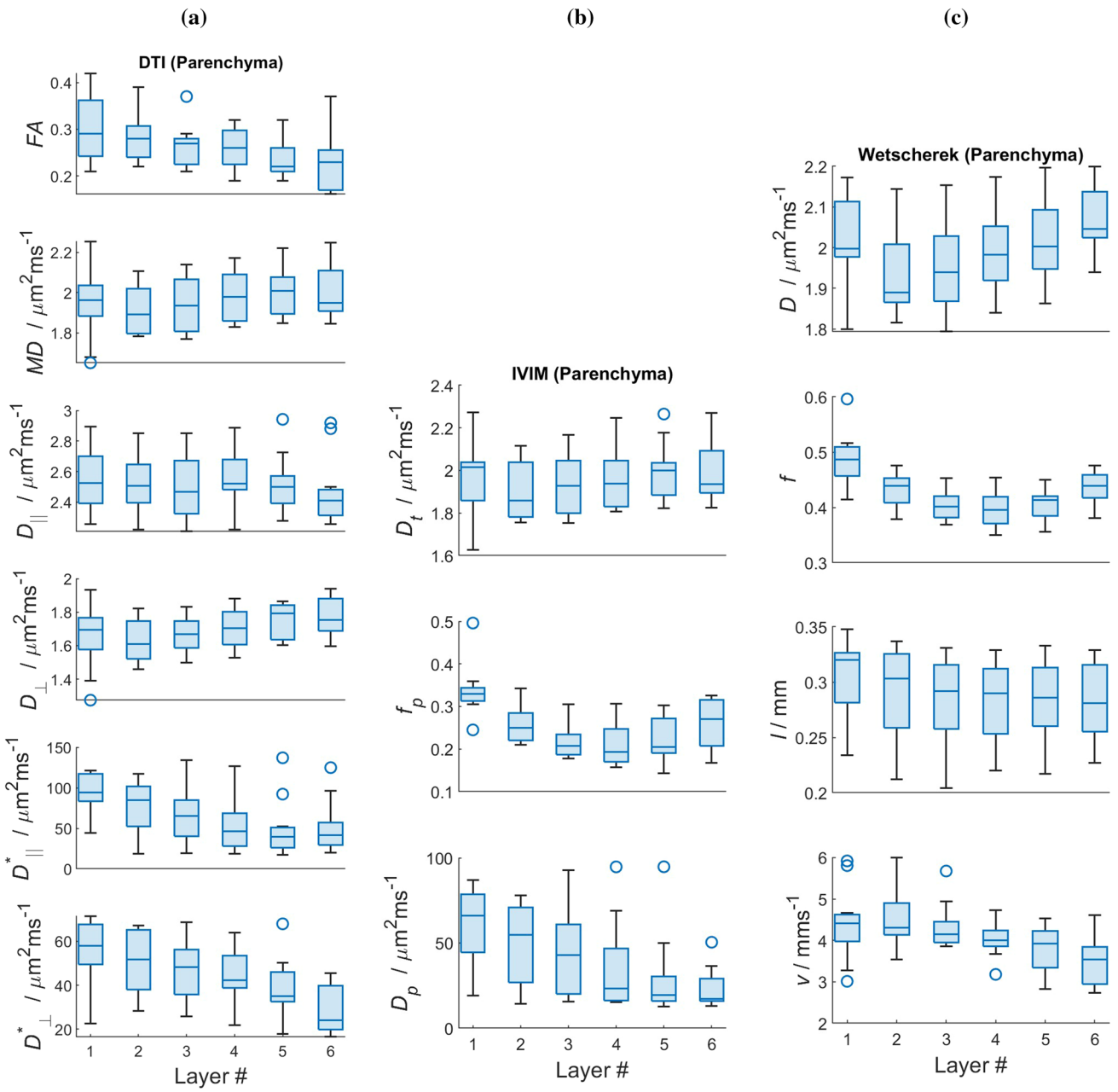

Fig. 3 Directional diffusion and flow parameters *MD*, *FA*, $D_{\parallel}$, $D_{\perp}$, $D^{*}_{\parallel}$, $D^{*}_{\perp}$ (**a**), IVIM parameters D_t, f_p, D_p (**b**), and FC-IVIM parameters *D*, *f*, *l*, *v* (**c**) vs. kidney layers containing both medulla and cortex

[43–46], 3D x-ray [47], and light sheet microscopy [48]. A potential transfer of this knowledge to in vivo human kidney imaging and extrapolations to its microstructure could be highly impactful in the study of renal dysfunction. However, diffusion-weighted MR parameters are generally not specific [49, 50] due to the dependency of the diffusion signal on different physiological parameters and restriction, as well as inter-species variations of microstructural features.

Accordingly, in the present study, we have scrutinized the dependence of renal DWI parameters from conventional representations (DTI, IVIM), an advanced hybrid DTI-IVIM approach [3, 51], and a multiple encoded FC-IVIM model [27] on concentric layers in vivo in humans. It is worthwhile to first summarize the correlation coefficients numerically and statistically to determine the strongest associations of DWI parameters with kidney layer. Secondly, we may hypothesize biophysical/microstructural features that are consistent with these trends, informed by known anatomy and histopathology. Regarding interpretation of the layer trends, we distinguish two

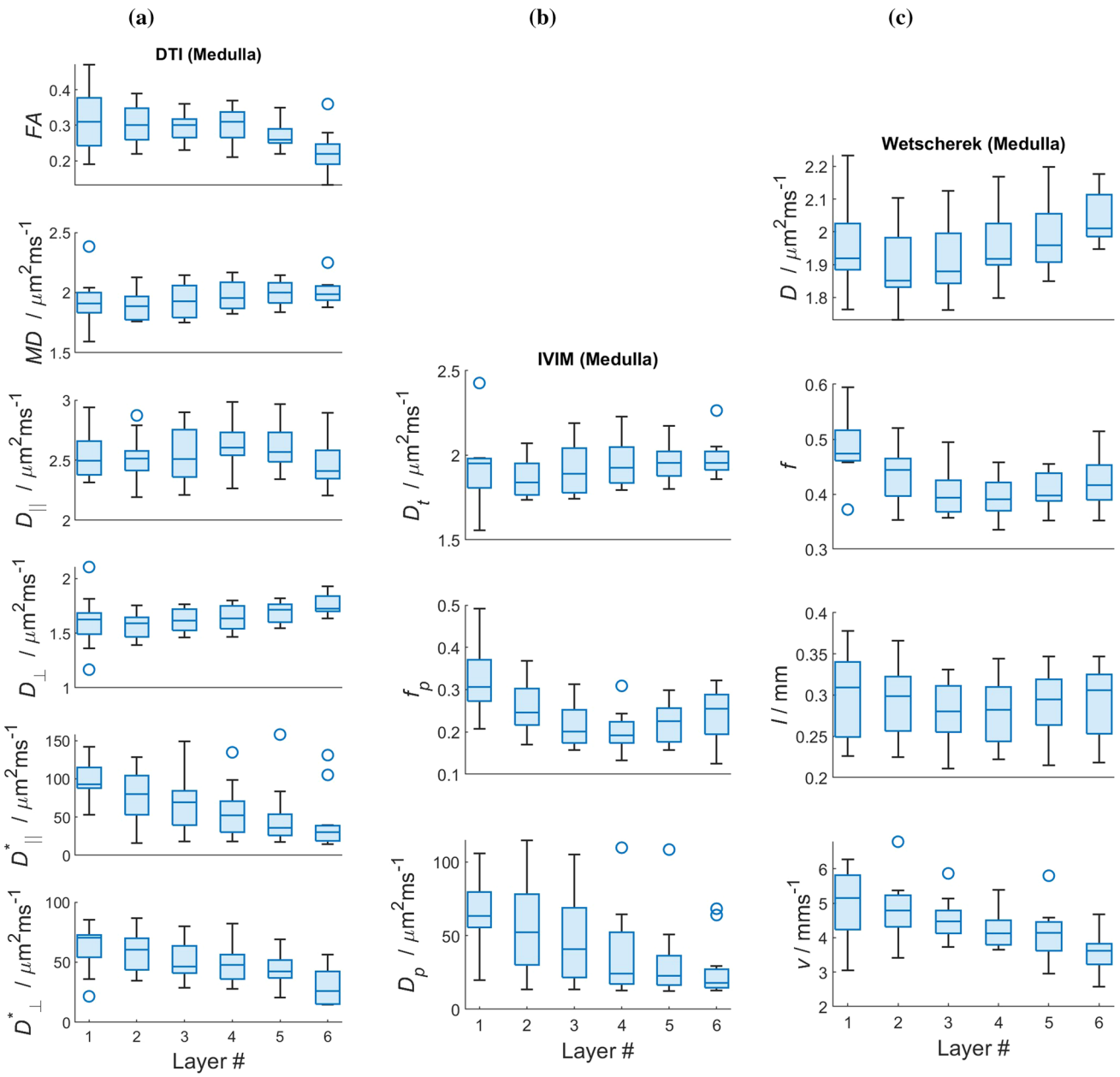

Fig. 4 Directional diffusion and flow parameters *MD*, *FA*, $D_{\parallel}$, $D_{\perp}$, $D^{*}_{\parallel}$, $D^{*}_{\perp}$ (**a**), IVIM parameters D_t, f_p, D_p (**b**), and FC-IVIM parameters *D*, *f*, *l*, *v* (**c**) vs. kidney layers in the medulla segmentations

different sources of layer dependence, as typically required in DWI multi-component modeling: (1) variations in diffusion coefficients and (2) variations in signal fraction of these components. For our purposes and with guidance from literature, the dominant components are (a) vascular, (b) tubular, and (c) interstitium and pathologically, fibrotic fraction. It is also important to note that the nephron path (through the glomerulus, proximal convoluted tubule, tubular loops of Henle, distal convoluted tubule, and collecting duct) proceeds back and forth between cortex and medulla rather than directly along the radial direction considered here. Thus, there is unavoidable averaging of multiple elements of the nephron within each layer.

As before, we summarize results in categories of structurally sensitive parameters and dynamic parameters. Assuming the tubular fraction dominates the structurally sensitive parameters' (*D*, MD, D_t, $D_{\perp}$) behavior, the decreasing trend from outer to inner layers may originate from a combination of factors. It is known that the tubular volume fraction decreases from 85% in cortex to 60% in the medulla [52, 53] and that in deeper layers a larger preponderance of thinner tubules (such as the loops of

Table 2 The Spearman correlations (r) and p-values characterize the association of parameters with layer index (1 = inner medulla; 6 = outer cortex)

Segmentation type	Model	Parameter	Spearman	
			r	p
Parenchyma	IVIM	D_t	0.128	0.307
		f_p	−0.378	0.002
		D_p	−0.52	< 0.001
	DTI	MD	0.185	0.137
		FA	−0.424	< 0.001
		$D_{\parallel}$	−0.108	0.388
		$D_{\perp}$	0.352	0.004
		$D^*_{\parallel}$	−0.462	< 0.001
		$D^*_{\perp}$	−0.549	< 0.001
	FC-IVIM	D	0.252	0.041
		f	−0.306	0.012
		l	−0.195	0.116
		v	−0.464	< 0.001
Medulla	IVIM	D_t	0.347	0.004
		f_p	−0.35	0.004
		D_p	−0.495	< 0.001
	DTI	MD	0.291	0.018
		FA	−0.371	0.002
		$D_{\parallel}$	0.011	0.928
		$D_{\perp}$	0.415	< 0.001
		$D^*_{\parallel}$	− 0.52	< 0.001
		$D^*_{\perp}$	−0.51	< 0.001
	FC-IVIM	D	0.347	0.004
		f	−0.364	0.003
		l	−0.061	0.625
		v	−0.535	< 0.001

The analysis was stratified by kidney segmentation type: parenchyma (including both cortex and medulla) or the medulla only, and included data from all 6 layers

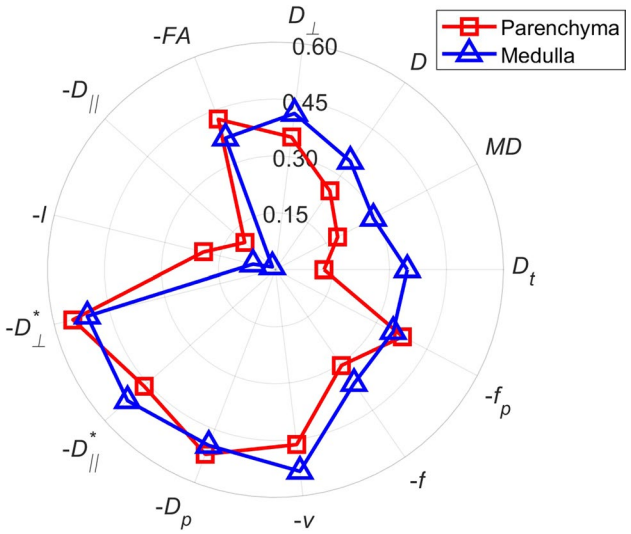

Fig. 5 Radar plot of Spearman correlation coefficients for each parameter, both the parenchymal (including both cortex and medulla) and the medulla only layers (i.e. an intersection of FA map and the layer masks). If the correlation coefficient was negative the parameter was marked with a negative meaning it would decrease from the inner to outer layers. Radius of each symbol depicts the magnitude of the spearman correlation coefficient r for parameter vs. layer

Henle) was found. Thus, larger average tubule diameters in outer cortical layers induce reduced diffusion restrictions. Finally, tubule and duct orientation become increasingly aligned in the medulla, driving the canonical feature of anisotropy (elevated FA and reduced $D_{\perp}$). $D_{\parallel}$ and multiple encoded FC-IVIM branching length l follow a relatively constant trend. A relatively constant $D_{\parallel}$, along with the known presence of tubules in all kidney layers, suggests diffusion is similarly hindered in the direction along the tubule axis (i.e. similar 'mean free path') in all layers. However, future studies similar to Scott et al. [54] might enable better quantification of the diffusion hindrance and branching length (l) using alternative modalities to test whether there are relatively fixed parameters across all kidney layers.

Intramedullary correlations were weaker for FA and l than for the full parenchyma; this may originate from a more homogeneous tissue sampling in the former case, in particular with regard to the diameter, degree of alignment, and vessel segment length of the tubular structures. However, it is notable that FA correlates strongly with layer in both parenchymal and medullary segmentations; the latter results suggest the limits of treating medulla as uniform entity such as in classical cortex and medulla segmentations.

The layered approach is analogous to the laminar analysis of the cortical gray matter [55] and superficial white matter [56]. However, within human kidneys, there are less distinct histological layers compared to cerebral tissue which complicates interpretations. Nevertheless, spatial profiling of DWI metrics throughout the kidney may ultimately yield more specific biomarkers of renal tissue microstructure. Further studies using in vivo and ex vivo DWI are required to establish their connection with human renal function and histology.

Regarding dynamics, a first-order physiological intuition about the dynamic IVIM parameters f_p and D_p, and FC-IVIM parameters f and flow velocity v would suggest that dynamics are slow in the inner layers since more exchange of water and other ions occurs between vascular and tubular spaces. However, the averaging of all dynamic flow systems (vasa recta, tubules, collecting ducts) must again be considered when interpreting the net higher flow rates evident in the inner radial layers. Nevertheless, one interesting result of this pilot application of the FC-IVIM model is that it prescribes the majority of this change to dynamics (velocity v)

and not to architecture (branching length l). Also, the slope of these variations of dynamic parameters (f_p, D_p, f, v) are more significant in the first three inner layers implying these flow describing parameters might be affected by the renal artery, vein, and pelvis. Conversely, in the outer layers which are mostly cortical tissue, there are networks of microvasculature and convoluted tubules with decreased velocities.

The FC-IVIM model is one of the few treatments of IVIM signal beyond the biexponential representation (e.g. [57–59]) and represents potential for biologic specificity. However, as with all diffusion MR models, it has its limitations, some of which might be better addressable in the future. First, the FC-IVIM model [27] assumes only one flow compartment with a single branching length and characteristic distribution of velocities, both of which are approximations. There are also no studies yet investigating numerical correlated errors between the model parameters velocity and branching length. These issues might result in biased outputs [50]. Again, further microstructural cross-validations are required for its features similar to the work by Scott et al. [54] where the branching length derivations of the model are compared with μCT measurements. Also, the analytical expressions and numerical phase distributions underlying the FC-IVIM model provide possibilities for the estimation of microstructural parameters from in vivo data. However, a study of the model estimates from simulated MR signals from Monte Carlo and/or particle trajectory simulation of water transport in relevant microstructural/microcirculatory networks (such as anisotropic flow networks as in renal medulla) might further illuminate its range of applicability. Interpretations of IVIM and DTI parameters would also benefit from such studies. Also, the multiple encodings required for the model should be considered in light of the balance between accuracy, precision, and clinically feasible scan times. A recent work has proposed optimized acquisitions with this in mind [31]. We did not employ these exact optimized acquisitions recommended in [31] but our acquisitions were somehow similar and near optimal in the case of b-values, diffusion times and pulse sequences used.

There are further limitations to this study. First, we have thus far collected the layer trends in young healthy subjects only, aiming to improve our understanding of the sources of diffusion MR signal in the kidneys. Hence, a natural future direction would be to test the layered analysis on DTI or IVIM parameters in chronic kidney disease patients or subjects with a wider range of ages [60]. However, a redefinition of the layers might be necessary in lesioned or morphologically abnormal kidneys. Finally, we did not perform a systematic variation of the number of layers chosen in our ROI sampling, nor did we perform an interreader comparison on their prescription.

In conclusion, we have performed a preliminary study on the dependence of a set of conventional and more advanced DWI derived parameters on concentric layers in healthy human kidneys. The most significant layer dependence was observed for pseudodiffusion parameters and structural fractional anisotropy, with weaker dependences observed for structural diffusivity parameters. Further validation of these trends in comparison with histologic reference, as well as correlation with measures of renal function, is required to improve our understanding of the sources of the diffusion signal in the kidneys. This knowledge might find translations into the clinics to optimize acquisition and better understand the pathophysiology of kidney diseases in the future.

Supplementary Information The online version contains supplementary material available at https://doi.org/10.1007/s10334-024-01159-6.

Acknowledgements This work was supported by the National Institutes of Health (NIH) (R01CA245671), and performed under the rubric of the Center for Advanced Imaging Innovation and Research (CAI^{2}R, www.cai2r.net), an NIBIB National Center for Biomedical Imaging and Bioengineering (NIH P41 EB017183).

Author contribution Nima Gilani: Methodology, Software, Writing-Original Draft. Artem Mikheev and Andreas Wetscherek: Software, Writing-Review & Editing. Inge M. Brinkmann and Thomas Benkert: Resources, Writing-Review & Editing. Dibash Basukala: Writing-Review & Editing. James S. Babb: Formal analysis. Malika Kumbella: Project administration. Hersh Chandarana: Writing-Review & Editing, Supervision, Funding acquisition. Eric E. Sigmund: Conceptualization, Investigation, Writing-Original Draft, Supervision, Funding acquisition.

Declarations

Conflict of interest Co-authors Inge M. Brinkmann, PhD and Thomas Benkert, PhD are employees of SIEMENS Healthineers.

Ethical standards All enrolled subjects provided written informed consent, and the ethics committee of our hospital approved this prospecrtive study (study number s20-01048).

References

1. Bane O, Seeliger E, Cox E, Stabinska J et al (2023) Renal MRI: from nephron to NMR signal. J Magn Reson Imaging 58:1660–1679
2. Le Bihan D (2019) What can we see with IVIM MRI? Neuroimage 187:56–67
3. Sigmund EE, Mikheev A, Brinkmann IM, Gilani N et al (2023) Cardiac phase and flow compensation effects on renal flow and microstructure anisotropy MRI in healthy human kidney. J Magn Reson Imaging 58(1):210–220
4. Gilani N (2024) Editorial for "Editorial for "Utility of prostate health index density for biopsy strategy in Biopsy-Naïve patients With PI-RADSv2.1 category 3 lesions". J Magn Reson Imaging. https://doi.org/10.1002/jmri.29269
5. Pierpaoli C (2010) Artifacts in diffusion MRI. In: DK Jones (ed) Diffusion MRI: theory, methods and applications. Oxford University Press, Oxford, pp 303–318

6. Gilani N, Mikheev A, Brinkmann IM, Basukala D et al (2023) Characterization of motion dependent magnetic field inhomogeneity for DWI in the kidneys. Magn Reson Imaging 100:93–101
7. Lanzman RS, Ljimani A, Muller-Lutz A, Weller J et al (2019) Assessment of time-resolved renal diffusion parameters over the entire cardiac cycle. Magn Reson Imaging 55:1–6
8. Ito K, Hayashida M, Kanki A, Yamamoto A et al (2018) Alterations in apparent diffusion coefficient values of the kidney during the cardiac cycle: evaluation with ECG-triggered diffusion-weighted MR imaging. Magn Reson Imaging 52:1–8
9. Wittsack HJ, Lanzman RS, Quentin M, Kuhlemann J et al (2012) Temporally resolved electrocardiogram-triggered diffusion-weighted imaging of the human kidney: correlation between intravoxel incoherent motion parameters and renal blood flow at different time points of the cardiac cycle. Invest Radiol 47(4):226–230
10. Milani B, Ledoux JB, Rotzinger DC, Kanemitsu M et al (2019) Image acquisition for intravoxel incoherent motion imaging of kidneys should be triggered at the instant of maximum blood velocity: evidence obtained with simulations and in vivo experiments. Magn Reson Med 81(1):583–593
11. Heusch P, Wittsack HJ, Kropil P, Blondin D et al (2013) Impact of blood flow on diffusion coefficients of the human kidney: a time-resolved ECG-triggered diffusion-tensor imaging (DTI) study at 3T. J Magn Reson Imaging 37(1):233–236
12. Gilani N, Mikheev A, Brinkmann IM, Basukala D et al (2023) The effect of cardiac gating on the repeatability of quantitative renal diffusion MRI. In: Proceedings of the International Society for Magnetic Resonance in Medicine, Toronto, Canada, p 1498
13. Heptinstall RH (2007) Heptinstall's pathology of the kidney, vol 1. Lippincott Williams & Wilkins, Philadelphia
14. Gilani N, Malcolm P, Johnson G (2017) A monte carlo study of restricted diffusion: implications for diffusion MRI of prostate cancer. Magn Reson Med 77(4):1671–1677
15. Gilani N, Malcolm P, Johnson G (2017) An improved model for prostate diffusion incorporating the results of monte carlo simulations of diffusion in the cellular compartment. NMR Biomed 30(12):e3782
16. Le Bihan D, Breton E, Lallemand D, Aubin ML, Vignaud J, Laval-Jeantet M (1988) Separation of diffusion and perfusion in intravoxel incoherent motion MR imaging. Radiology 168(2):497–505
17. Thoeny HC, Keyzer FD (2011) Diffusion-weighted MR Imaging of native and transplanted kidneys. Radiology 259(1):25–38
18. Zhang JL, Sigmund EE, Chandarana H, Rusinek H et al (2010) Variability of renal apparent diffusion coefficients: limitations of the monoexponential model for diffusion quantification. Radiology 254(3):783–792
19. Ljimani A, Caroli A, Laustsen C, Francis S et al (2020) Consensus-based technical recommendations for clinical translation of renal diffusion-weighted MRI. MAGMA 33(1):177–195
20. Caroli A, Schneider M, Friedli I, Ljimani A et al (2018) Diffusion-weighted magnetic resonance imaging to assess diffuse renal pathology: a systematic review and statement paper. Nephrol Dial Transplant 33(2S):ii29–ii40
21. Ries M, Jones RA, Basseau F, Moonen CT, Grenier N (2001) Diffusion tensor MRI of the human kidney. J Magn Reson Imaging JMRI 14(1):42–49
22. Periquito JS, Gladytz T, Millward JM, Delgado PR et al (2021) Continuous diffusion spectrum computation for diffusion-weighted magnetic resonance imaging of the kidney tubule system. Quant Imaging Med Surg 11(7):3098–3119
23. van Baalen S, Leemans A, Dik P, Lilien MR, Ten Haken B, Froeling M (2017) Intravoxel incoherent motion modeling in the kidneys: comparison of mono-, bi-, and triexponential fit. J Magn Reson Imaging 46(1):228–239
24. Notohamiprodjo M, Chandarana H, Mikheev A, Rusinek H et al (2014) Combined intravoxel incoherent motion and diffusion tensor imaging of renal diffusion and flow anisotropy. Magn Reson Med. https://doi.org/10.1002/mrm.25245
25. Hilbert F, Bock M, Neubauer H, Veldhoen S et al (2016) An intravoxel oriented flow model for diffusion-weighted imaging of the kidney. NMR Biomed 29(10):1403–1413
26. Van Phi VD, Becker AS, Ciritsis A, Reiner CS, Boss A (2018) Intravoxel incoherent motion analysis of abdominal organs: application of simultaneous multislice acquisition. Invest Radiol 53(3):179–185
27. Wetscherek A, Stieltjes B, Laun FB (2015) Flow-compensated intravoxel incoherent motion diffusion imaging. Magn Reson Med 74(2):410–419
28. Stabinska J, Ljimani A, Zollner HJ, Wilken E et al (2021) Spectral diffusion analysis of kidney intravoxel incoherent motion MRI in healthy volunteers and patients with renal pathologies. Magn Reson Med 85(6):3085–3095
29. Basser PJ, Pierpaoli C (1996) Microstructural and physiological features of tissues elucidated by quantitative-diffusion-tensor MRI. J Magn Reson Ser B 111(3):209–219
30. Lemberskiy G, Rosenkrantz AB, Veraart J, Taneja SS, Novikov DS, Fieremans E (2017) Time-dependent diffusion in prostate cancer. Invest Radiol 52(7):405–411
31. Gurney-Champion OJ, Rauh SS, Harrington K, Oelfke U, Laun FB, Wetscherek A (2020) Optimal acquisition scheme for flow-compensated intravoxel incoherent motion diffusion-weighted imaging in the abdomen: an accurate and precise clinically feasible protocol. Magn Reson Med 83(3):1003–1015
32. Piskunowicz M, Hofmann L, Zuercher E, Bassi I et al (2015) A new technique with high reproducibility to estimate renal oxygenation using BOLD-MRI in chronic kidney disease. Magn Reson Imaging 33(3):253–261
33. Milani B, Ansaloni A, Sousa-Guimaraes S, Vakilzadeh N et al (2017) Reduction of cortical oxygenation in chronic kidney disease: evidence obtained with a new analysis method of blood oxygenation level-dependent magnetic resonance imaging. Nephrol Dial Transplant 32(12):2097–2105
34. Li LP, Milani B, Pruijm M, Kohn O et al (2020) Renal BOLD MRI in patients with chronic kidney disease: comparison of the semi-automated twelve layer concentric objects (TLCO) and manual ROI methods. MAGMA 33(1):113–120
35. Zhao K, Li S, Liu Y, Li Q et al (2023) Diagnostic and prognostic performance of renal compartment volume and the apparent diffusion coefficient obtained from magnetic resonance imaging in mild, moderate and severe diabetic kidney disease. Quant Imaging Med Surg 13(6):3973–3987
36. Sanmiguel Serpa LC, De Visschere P, Speeckaert M, Pullens P (2023) A new method to analyse renal perfusion: a proof of concept. In: Proceedings of the International Society for Magnetic Resonance in Medicine, Toronto, Canada, p 3803
37. Veraart J, Fieremans E, Novikov DS (2016) Diffusion MRI noise mapping using random matrix theory. Magn Reson Med 76(5):1582–1593
38. Smith SM, Jenkinson M, Woolrich MW, Beckmann CF et al (2004) Advances in functional and structural MR image analysis and implementation as FSL. Neuroimage 23(1S):S208–S219
39. Führes T, Saake M, Szczepankiewicz F, Bickelhaupt S, Uder M et al (2023) Impact of velocity- and acceleration-compensated encodings on signal dropout and black-blood state in diffusion-weighted magnetic resonance liver imaging at clinical TEs. PLOS ONE 18(10):e0291273. https://doi.org/10.1371/journal.pone.0291273
40. Jones DK, Basser PJ (2004) "Squashing peanuts and smashing pumpkins": how noise distorts diffusion-weighted MR data. Magn Reson Med 52(5):979–993
41. Hirsch JG, Schwenk SM, Rossmanith C, Hennerici MG, Gass A (2003) Deviations from the diffusion tensor model as revealed by

contour plot visualization using high angular resolution diffusion-weighted imaging (HARDI). MAGMA 16(2):93–102
42. Funck C, Laun FB, Wetscherek A (2018) Characterization of the diffusion coefficient of blood. Magn Reson Med 79(5):2752–2758
43. Johnson GA, Benveniste H, Black RD, Hedlund LW, Maronpot RR, Smith BR (1993) Histology by magnetic resonance microscopy. Magn Reson Q 9(1):1–30
44. de Rochefort L, Liu T, Kressler B, Liu J et al (2010) Quantitative susceptibility map reconstruction from MR phase data using bayesian regularization: validation and application to brain imaging. Magn Reson Med 63(1):194–206
45. Xie L, Bennett KM, Liu C, Johnson GA, Zhang JL, Lee VS (2016) MRI tools for assessment of microstructure and nephron function of the kidney. Am J Physiol Renal Physiol 311(6):F1109–F1124
46. Morozov D, Parvin N, Charlton JR, Bennett KM (2021) Mapping kidney tubule diameter ex vivo by diffusion MRI. Am J Physiol Renal Physiol 320(5):F934–F946
47. Taphorn K, Busse M, Brantl J, Gunther B et al (2022) X-ray stain localization with near-field ptychographic computed tomography. Adv Sci (Weinh) 9(24):e2201723
48. Puelles VG, Combes AN, Bertram JF (2021) Clearly imaging and quantifying the kidney in 3D. Kidney Int 100(4):780–786
49. Jones DK, Knosche TR, Turner R (2013) White matter integrity, fiber count, and other fallacies: the do's and don'ts of diffusion MRI. Neuroimage 73:239–254
50. Afzali M, Pieciak T, Newman S, Garyfallidis E et al (2021) The sensitivity of diffusion MRI to microstructural properties and experimental factors. J Neurosci Methods 347:108951
51. Liu AL, Mikheev A, Rusinek H, Huang WC et al (2018) REnal flow and microstructure anisotroPy (REFMAP) MRI in normal and peritumoral renal tissue. J Magn Reson Imaging 48(1):188–197
52. Fioretto P, Sutherland DER, Najafian B, Mauer M (2006) Remodeling of renal interstitial and tubular lesions in pancreas transplant recipients. Kidney Int 69(5):907–912
53. Kriz W, Napiwotzky P (1979) Structural and functional aspects of the renal interstitium. Contrib Nephrol 16:104–108
54. Scott LA, Dickie BR, Rawson SD, Coutts G et al (2021) Characterisation of microvessel blood velocity and segment length in the brain using multi-diffusion-time diffusion-weighted MRI. J Cereb Blood Flow Metab 41(8):1939–1953
55. Gilani N, Hildebrand S, Schueth A, Roebroeck A (2019) Monte Carlo simulation of diffusion MRI in geometries constructed from two-photon microscopy of human cortical grey matter. bioRxiv. https://doi.org/10.1101/626945
56. Kirilina E, Helbling S, Morawski M, Pine K et al (2020) Superficial white matter imaging: contrast mechanisms and whole-brain in vivo mapping. Sci Adv 6(41):eaaz9281
57. Ahlgren A, Knutsson L, Wirestam R, Nilsson M et al (2016) Quantification of microcirculatory parameters by joint analysis of flow-compensated and non-flow-compensated intravoxel incoherent motion (IVIM) data. NMR Biomed 29(5):640–649
58. Fournet G, Li JR, Cerjanic AM, Sutton BP, Ciobanu L, Le Bihan D (2017) A two-pool model to describe the IVIM cerebral perfusion. J Cereb Blood Flow Metab 37(8):2987–3000
59. Kennan RP, Gao JH, Zhong J, Gore JC (1994) A general model of microcirculatory blood flow effects in gradient sensitized MRI. Med Phys 21(4):539–545
60. Weinstein JR, Anderson S (2010) The aging kidney: physiological changes. Adv Chronic Kidney Dis 17(4):302–307